Contents lists available at ScienceDirect

Transactions of Nonferrous Metals Society of China

36(2026) 244−258

www.tnmsc.cn

Effect of active metal oxide dopants on wettability and interfacial reaction between K417G superalloy and Al_2O_3-based ceramic shell

Bao-hong KOU [a,b,c], Wen-tao ZHOU [a,b,c], Yong-hui PENG [a,b,c], Jing OUYANG [a,b,c,*]

[a] Department of Inorganic Materials, School of Minerals Processing and Bioengineering, Central South University, Changsha 410083, China;

[b] Hunan Key Lab of Mineral Materials and Application, Central South University, Changsha 410083, China;

[c] Engineering Research Center of Ministry of Education for Carbon Emission Reduction in Metal Resource Exploitation and Utilization, Central South University, Changsha 410083, China

Abstract: Some active metal oxides (Al_2O_3, TiO_2, and Cr_2O_3) were selected as dopants to the Al_2O_3-based ceramic shells for investment casting of K417G superalloy. The effects of dopant types and contents (0, 2, 5, and 8 wt.%) on the wettability and interfacial reaction between the alloy and shell were investigated by a sessile-drop experiment. The results show that increasing the Al_2O_3 doping contents (0−8 wt.%) reduces the porosity (21.74%−10.08%) and roughness (3.22−1.34 μm) of the shell surface. The increase in Cr_2O_3 dopant content (2−8 wt.%) further exacerbates the interfacial reaction, leading to an increase in the thickness of the reaction layer (2.6−3.1 μm) and a decrease in the wetting angle (93.9°−91.0°). The addition of Al_2O_3 and TiO_2 dopants leads to the formation of Al_2TiO_5 composite oxides in the reaction products, which effectively inhibits the interfacial reaction. The increase in TiO_2 dopant contents (0−8 wt.%) further promotes the formation of Al_2TiO_5, which decreases the thickness of the interfacial reaction layer (3.9−1.2 μm) and increases the wetting angle (95.0°−103.8°). The introduced dopants enhance the packing density of the shell surface, while simultaneously suppress the diffusion of active metal elements from the alloy matrix to the interface.

Keywords: Al_2O_3-based ceramic shell; K417G superalloy; metal oxide dopants; interfacial reaction; wettability

1 Introduction

Investment casting technology [1,2] enables the near-net-shape formation of complex components, making it the primary method for manufacturing high-melting-point, lightweight, and intricately structured Ni-based superalloy blades [3]. However, the interfacial reaction between the molten alloy and the ceramic shell during the casting process can lead to surface defects such as sticking sand and blowholes, which negatively impact the fatigue performance and mechanical properties of the blades [4,5]. These defects typically require secondary processing (e.g., sandblasting, grinding, and polishing) for removal, which increases production costs and even causes recrystallization, ultimately reducing the service life of the blades [6,7].

The interfacial reaction often happens between active metal elements in the molten alloys (e.g., Al, Ti, Cr, and Hf) and oxides in ceramic shell (e.g., Al_2O_3, SiO_2, Na_2O, and Fe_2O_3) [8−10], resulting in the formation of more stable oxides (e.g., Al_2O_3, Cr_2O_3, and HfO_2) and composite oxides (e.g., $(Al_{1-x}Cr_x)_2O_3$) [11−13]. The wettability between them represents the spreading behavior of the molten alloys on the shell surface, which indicates the extent of the interfacial reaction [10]. Proper wettability

Corresponding author: *Jing OUYANG, Tel: +86-731-88830549, E-mail: jingouyang@csu.edu.cn

https://doi.org/10.1016/S1003-6326(25)66961-5

Received 25 April 2024; accepted 10 January 2025

promotes uniform spreading of the molten alloy, thereby reducing surface defects. In contrast, excessive wettability can exacerbate the interfacial reaction, leading to the formation of harmful phases [13]. Currently, the sessile-drop experiment is usually adopted to evaluate the wettability and interfacial reaction, as it can directly measure the wetting angle and hence facilitate the analysis of reaction products [14]. The wettability and interfacial reaction are primarily influenced by the composition of both the superalloy and the ceramic shell. Therefore, studying the relationship between wettability and interfacial reactions is essential for improving the surface quality of the cast products.

Previous studies have investigated the effects of alloy composition on wettability and interfacial reaction [15−18]. LI et al [16] found that reducing impurities (O, N, and S) in the DZ125 superalloy decreases the thickness of interfacial reaction layer while increasing the wetting angle. ZI et al [17,18] regulated the wettability and interfacial reaction between the Ni-based superalloy and the Al_2O_3-based ceramic shell by adding Re and Y into the alloy matrix. The results showed that, the extent of interfacial reaction reduced, and the wetting angle increased when the Re content increased. When the Re content reached 6 wt.%, the displacement reaction between Hf in the molten alloy and SiO_2 in the shell was completely inhibited [17]. As the Y content increased, the extent of the interfacial reaction was intensified, and the wetting angle decreased. The Y in the molten alloy reacted with the Al_2O_3 and SiO_2 in the shell to form Y_2O_3 and Y_2O_3−Al_2O_3 composite oxides [18]. Similarly, the composition of the ceramic shell not only influences the wettability and interfacial reaction, but also changes the composition of the alloy surface [19−22]. ДЕМНИС et al [21] found that the interfacial reaction increased the Cr content in the ceramic shell from 0.2% to 1.2%, leading to a Cr deficiency on the alloy surface. So, pre-absorption of a certain amount of Cr on the surface of ceramic shell could suppress the diffusion of Cr from the alloy matrix. SHI et al [22] found that the addition of Cr_2O_3 particles enhanced the density of the shell surface and formed an Al_2O_3−Cr_2O_3−SiO_2 composite oxide, which inhibited the interfacial reaction.

Despite these advancements, systematic research on the effects of ceramic shell composition on wettability, interfacial reaction, and changes in active metal elements are rarely reported. As a result, this work introduced some active metal oxides as dopants into a stereotype Al_2O_3-based ceramic shell to enhance the packing density of the shell surface, and to suppress the diffusion of active metal elements from the alloy matrix to the interface. The effects of dopant types and contents on wettability and interfacial reaction were studied through a sessile-drop experiment, and the reaction products were analyzed to elucidate the mechanisms underlying the acquired results. The findings of this work are crucial for designing some advanced ceramic shells, and for developing precision casting technology.

2 Experimental

2.1 Composition design of Al_2O_3-based ceramic shell

In this study, K417G superalloy was used as the research material (with composition (wt.%): Al 4.80−5.70, Ti 4.10−4.70, Cr 8.50−9.50, Co 9.00−11.0, Mo 2.50−3.50, C 0.13−0.22, Zr 0.05−0.09, O 0.0006, N 0.0002, S <0.0004, and Ni Bal.). The primary components of the Al_2O_3-based ceramic shell surface are Al_2O_3 (fused corundum) and SiO_2 (silica sol) [16,17]. The interfacial reaction is assumed to arise from the oxidation of active elements in the alloy [23,24]. Therefore, the thermodynamic stability of the oxides of these elements was used to evaluate their involvement in the interfacial reaction [25]. Notably, the stability of each element can only be compared when it reacts with 1 mol O_2 to form the corresponding oxides (with equivalent oxygen content) [26]. Figure 1 shows the temperature-dependent trend of the standard Gibbs free energy change (ΔG) for potential oxide formation in the interfacial reaction system between the K417G superalloy and Al_2O_3-based ceramic shell [27]. Within the temperature range of 1000−2000 K, the thermal stability of the oxides follows the order: Al_2O_3 > TiO_2 > SiO_2 > Cr_2O_3 > MoO_3 > CoO > NiO. Thus, the relative reactivity of the alloying elements can be ranked as follows: Al > Ti > Cr > Mo > Co > Ni. Based on this calculation, Al_2O_3, TiO_2, and Cr_2O_3 fine particles were selected as dopants for the shell. On one hand, the addition of dopant particles can enhance the packing density of the shell surface, thereby reducing thermal erosion caused by the molten alloy. On the other hand, the

dopants enable the shell to pre-absorb active metal elements, which suppresses their diffusion from the alloy matrix to the interface area, and also inhibits the interfacial reactions.

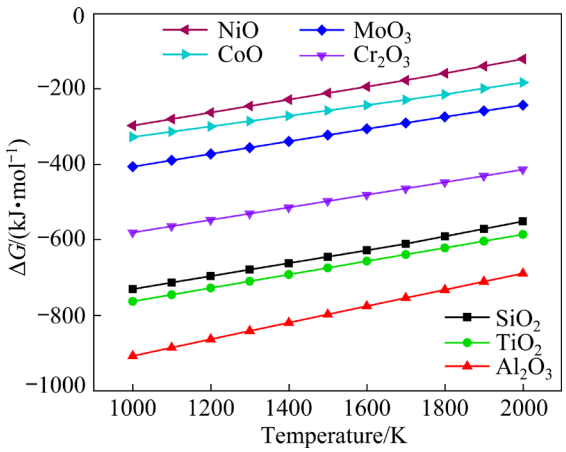

Fig. 1 Gibbs free energy change (ΔG) of different oxides in alloy/shell interfacial reaction system

The Al_2O_3-based ceramic shell was fabricated by the lost wax method [16,17]. The slurry used for shell production comprised fused corundum (refractory material), silica sol (binder), and dopant particles, with a mass ratio of fused corundum to silica sol of 3∶1. The dopant content was determined based on its proportion to the fused corundum. The sample names and their corresponding dopant contents are given in Table 1, while the composition and particle size information of the raw materials are detailed in Table 2. After thoroughly mixing the slurry, the wax mold underwent a cyclic processes of slurry coating, stuccoing, and drying, and these processes were repeated for many times until the shell reached a thickness of 6 mm. The molds were then dewaxed at 473 K (200 °C) for 2 h and sintered at 1223 K (950 °C) for 2 h, after which the shells were cut into 20 mm × 20 mm × 6 mm blocks using diamond wire cutting.

Table 1 Sample and corresponding dopant contents

Sample	Dopant	Content/wt.%
FC	–	–
2Cr-FC	Cr_2O_3	2
5Cr-FC		5
8Cr-FC		8
2Al-FC	Al_2O_3	2
5Al-FC		5
8Al-FC		8
2Ti-FC	TiO_2	2
5Ti-FC		5
8Ti-FC		8

Table 2 Composition of raw materials in preparing ceramic shell

Material	Powder	Size/μm	Composition or content/wt.%
Refractory	Fused corundum	45	Al_2O_3 99.28, SiO_2 0.41, CaO 0.03, Fe_2O_3 0.04, Na_2O 0.15, Loss 0.09
Dopant	Cr_2O_3	1−3	Cr_2O_3 ≥99.9, Loss ≤0.1
	Al_2O_3	1−5	Al_2O_3 ≥99.9, Loss ≤0.1
	TiO_2	1−3	TiO_2 ≥99.9, Loss ≤0.1
Binder	Silica solution	–	SiO_2 30, water bal.

2.2 Sessile-drop experiment

The sessile-drop experiment [18] was performed in a vacuum induction directional solidification furnace to study the wettability and interfacial reaction between the K417G superalloy and the Al_2O_3-based ceramic shell at high temperatures. The experimental setup is presented in Fig. 2(a). Firstly, the K417G superalloy was cut into 5 mm × 5 mm × 5 mm blocks using electric discharge machining, polished with sandpaper to obtain a smooth and bright surface, and then ultrasonically cleaned in anhydrous ethanol to remove surface oils and impurities. A ceramic bracket was placed on the water-cooled crystallizer within the furnace. The alloy block and ceramic shell were placed on the bracket in a sealed furnace, and then the bracket was lifted into the graphite electrode. The pressure in the furnace was reduced to 5×10^{-2} Pa. The furnace temperature was then increased from 20 °C (293 K) to 1350 °C (1623 K) at a heating rate of 40 °C/min [28], where it was held for 40 min to melt the alloy block into a nearly spherical droplet (Fig. 2(b)). Finally, the power of furnace was turned off, allowing the alloy droplet to solidify as it cooled within the furnace, thereby obtaining the final samples. The wetting angle is calculated using the following equation [29]:

$$\theta=2\arctan(2h/d) \quad (1)$$

where θ represents the actual contact angle (wetting angle) between the alloy droplet and the ceramic shell, h is the droplet height, and d is the bottom diameter of the droplet. These dimensions were

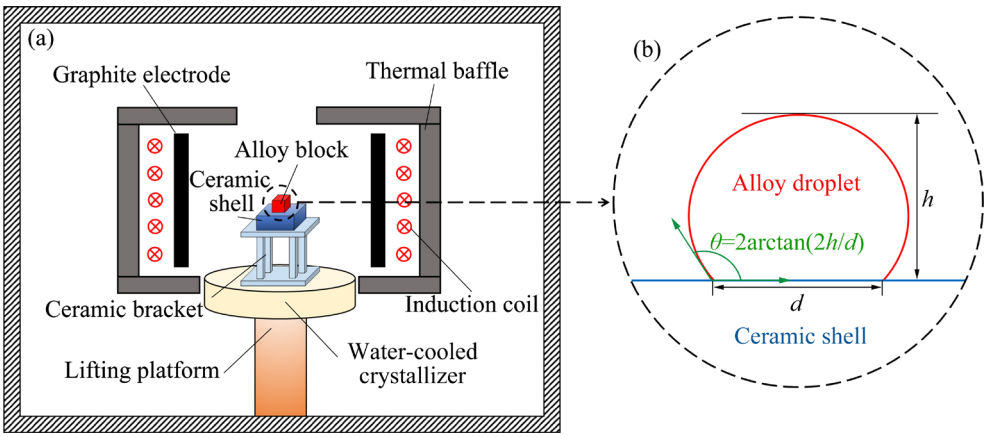

Fig. 2 Schematic diagram: (a) Experimental setup; (b) Method for measuring wetting angle

measured using a vernier caliper. To ensure experimental accuracy, the final wetting angle value was calculated as the average of five independent measurements.

2.3 Characterization methods

Surface morphology of the shell was observed by scanning electron microscopy (SEM, CLARA, TESCAN, Czech Republic), the porosity was calculated using Image-Pro software, and the roughness was measured with a 3D profiler (GT-K 3D, Bruker, Germany). After the sessile-drop experiment, the front view of each sample was captured using a camera (EOS-M50, Canon, Japan). Micro-area X-ray diffraction (XRD, Bruker D8 Advance, Germany) was used to analyze the phase composition of the reaction products on the alloy and shell surfaces. The micro-morphology of the alloy and shell surfaces was observed by SEM, and the chemical composition was analyzed by energy-dispersive spectrometer (EDS, Xplore 30). The alloy droplets were sectioned perpendicular to the interfacial reaction layer and prepared as metallographic samples. Subsequently, the micro-morphology and elemental distribution of the interfacial reaction layer on the alloy surface were examined by SEM and EDS. Finally, X-ray photoelectron spectroscopy (XPS, Thermo Scientific K-Alpha, USA) was used to analyze the elemental valence states of the reaction products.

3 Results and discussion

3.1 Effect of dopant content on shell morphology, porosity, and roughness

In sintering process, water evaporates from the shell surface, resulting in a porous structure [28], which allows the molten alloy to penetrate the surface pores through capillary effect, leading to thermal erosion by the molten alloy [16,17]. The microstructure of the shell surface (Figs. 3(a_1−d_1)) and its 3D contour (Figs. 3(a_2−d_2)) illustrate an obvious change with the increase of Al_2O_3 dopant content. The corresponding porosity and roughness values (Fig. 4) clearly demonstrate that the incorporation of dopant particles modifies the microstructure of the shell surface. A significant enhancement in the density of the shell surface increases with the dopant content (0, 2, 5, and 8 wt.%), which is attributed to the filling of large pores on shell surface by small dopant particles, where the porosity decreases from 21.74% to 10.08%, and roughness diminishes from 3.22 to 1.34 μm. As the particle size of the other dopants is even slightly smaller than that of the Al_2O_3 (Table 2), this inevitably results in a similar effect with that of Al_2O_3 on density of the shell surfaces.

3.2 Effect of dopant type and content on wettability and interfacial reaction

Figure 5(a) shows the front view of samples after the sessile-drop experiment. Figure 5(b) presents the longitudinal profile microstructure of the alloy surface. The wetting angle and the thickness of the interfacial reaction layer are calculated based on these observations (Fig. 6). The results of the sessile-drop experiment indicate that the alloy block melts at high temperatures, forming nearly spherical droplets on the shell surface, and the dopants significantly affect the wetting angle and thickness of the interfacial reaction layer. In the FC

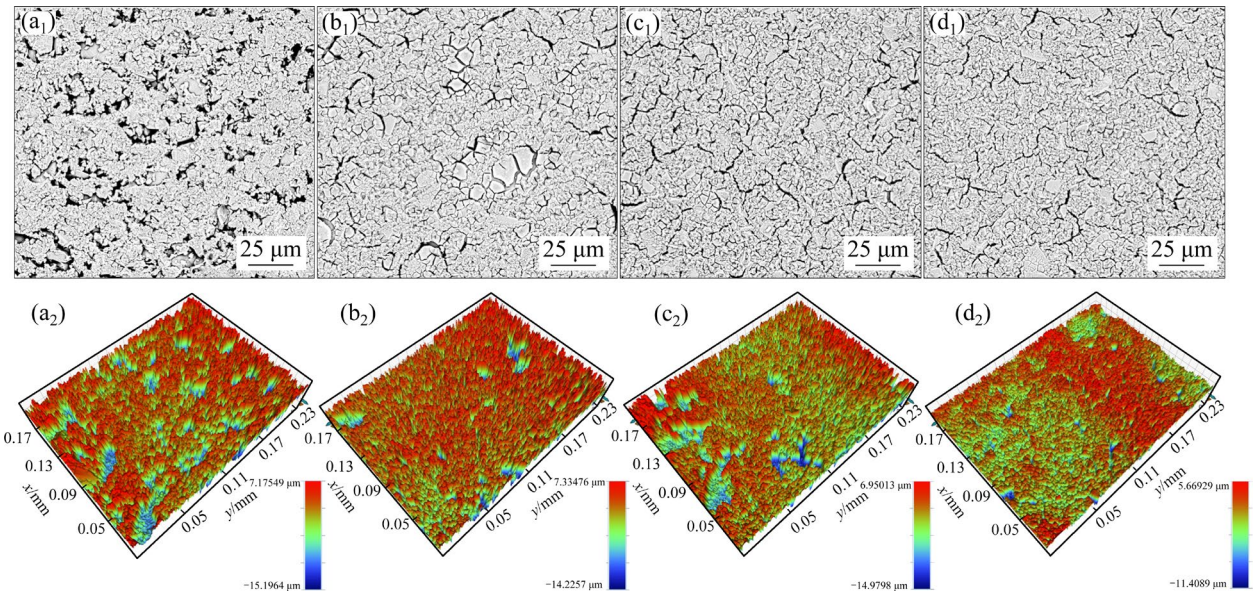

Fig. 3 Micro-morphology (a_1−d_1) and 3D profile (a_2−d_2) of shell surface with different Al_2O_3 dopant contents: (a_1, a_2) 0; (b_1, b_2) 2 wt.%; (c_1, c_2) 5 wt.%; (d_1, d_2) 8 wt.%

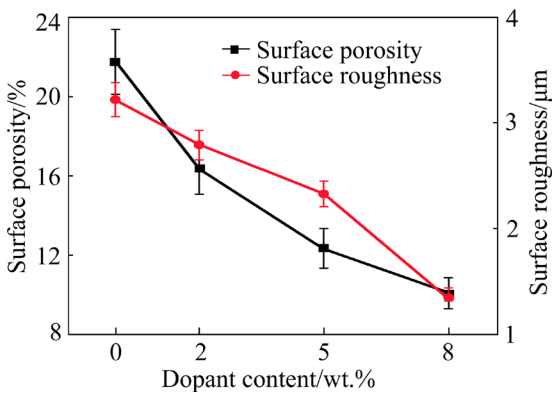

Fig. 4 Porosity and roughness of shell surface with different Al_2O_3 dopant contents

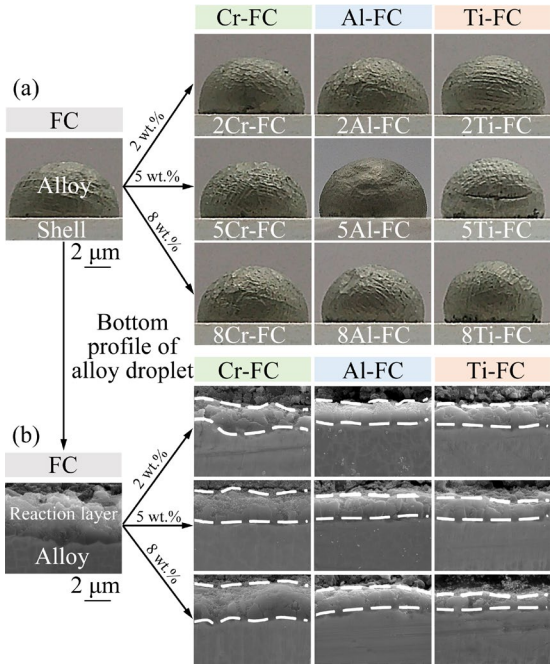

Fig. 5 Sessile-drop experiment results: (a) Front view of each sample; (b) Micro-morphology of longitudinal profile on alloy surface

sample, the wetting angle is approximately 95.0°, and the thickness of interfacial reaction layer is about 3.9 μm. As the Cr_2O_3 dopant content increases (2, 5, and 8 wt.%), wetting angle decreases (93.9°, 92.1° and 91.0°), while the thickness of interfacial reaction layer increases (2.6, 2.9 and 3.1 μm). In contrast, increasing the Al_2O_3 dopant contents (2, 5, and 8 wt.%) results in an increase in the wetting angle (96.2°, 97.1° and 99.4°) and a decrease in the thickness of interfacial reaction layer (2.3, 2.2 and 2.1 μm). Similarly, with the increase of TiO_2 dopant content (2, 5, and 8 wt.%), the wetting angle increases (98.8°, 100.6° and 103.8°), while thickness of the interfacial reaction layer decreases (2.0, 1.5 and 1.2 μm).

3.3 Phase composition and morphology of reaction products with different dopants

Due to the low density of the shell surface in the FC sample (Figs. 3 and 4), the molten alloy experiences very severe thermal erosion, leading to the most intense interfacial reaction and the largest thickness of the interfacial reaction layer (Figs. 5 and 6). The reaction products (Fig. 7(a)) on the alloy

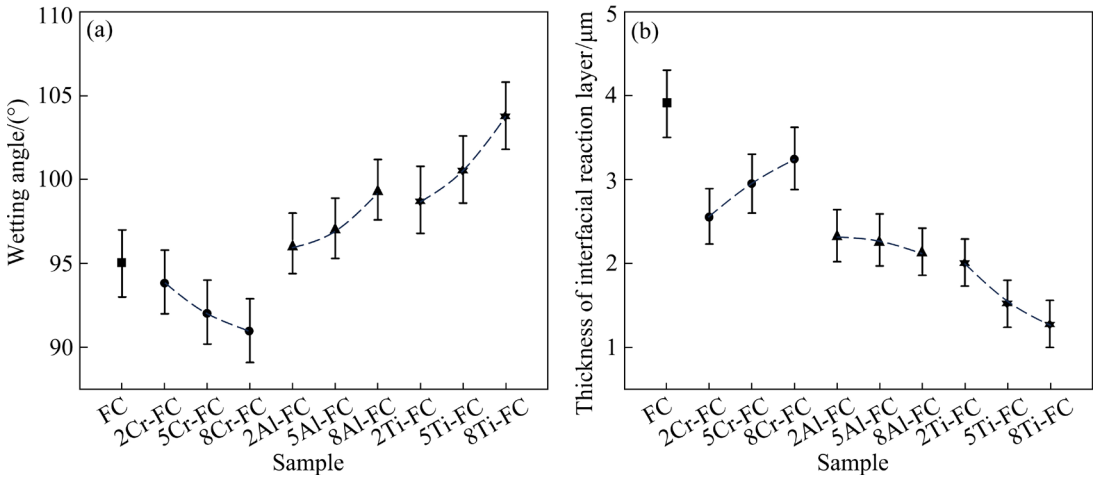

Fig. 6 Sessile-drop experiment results of samples with different dopants in ceramic shell: (a) Wetting angle; (b) Thickness of interfacial reaction layer

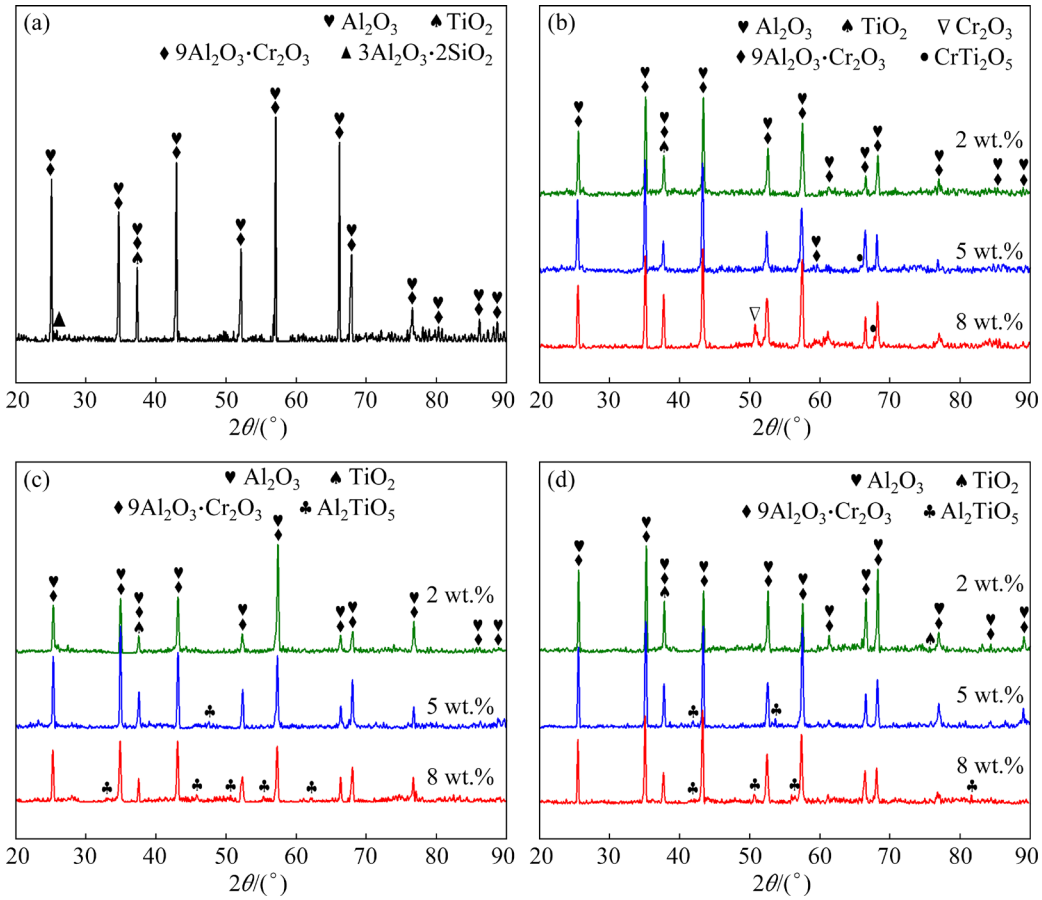

Fig. 7 XRD patterns of reaction products on alloy surface: (a) FC; (b) Cr-FC; (c) Al-FC; (d) Ti-FC

surface in the FC sample contains Cr_2O_3, Al_2O_3, TiO_2, mullite ($3Al_2O_3{\cdot}2SiO_2$), and $9Al_2O_3{\cdot}Cr_2O_3$. Some other potential reaction products may exist in the shell but they cannot be detected due to the very small quantity in the raw sources and products. The mullite and $9Al_2O_3{\cdot}Cr_2O_3$ phases are formed following Eq. (2) [29] and Eq. (3) [22] in the high-temperature circumstance:

$$3Al_2O_3+2SiO_2=3Al_2O_3{\cdot}2SiO_2 \quad (2)$$

$$9Al_2O_3+Cr_2O_3=9Al_2O_3{\cdot}Cr_2O_3 \quad (3)$$

Figure 7(b) shows that when the Cr_2O_3 dopant

content is 2 wt.%, the phase composition on alloy surface is the same as that of the FC sample. However, when the Cr_2O_3 dopant content increases from 5 wt.% to 8 wt.%, diffractions from Cr_2O_3 and the $CrTi_2O_5$ are observed. Although the Cr_2O_3 dopant enhances the density of the shell surface, its lower thermal stability (Fig. 1) allows it to react with the active metal elements in the molten alloy, resulting in the formation of $CrTi_2O_5$ composite oxides. Some Cr_2O_3 does not participate in the reaction, resulting in the observation of single Cr_2O_3 phase. In contrast, the Al_2O_3 and TiO_2 dopants have higher thermal stability compared to Cr_2O_3, making them less reactive with the molten alloy. Notably, the presences of Al_2O_3 and TiO_2 dopants lead to the formation of Al_2TiO_5 composite oxides in the reaction products (Figs. 7(c, d)). When the TiO_2 dopant content reaches 8 wt.%, a diffraction from Al_2TiO_5 appears at 2θ=81.8°, indicating that TiO_2 dopant is favorable for the formation of Al_2TiO_5 composite oxides.

Figures 8 and 9 illustrate the micro-morphology and elemental distribution on the alloy surfaces (Fig. 8) and shell surfaces (Fig. 9) of FC, 8Cr-FC, 8Al-FC, and 8Ti-FC samples. The interfacial reaction leads to the formation of reaction products on both the alloy and shell surfaces (Figs. 8(a) and 9(a)). These products are primarily composed of Al_2O_3 (dark gray area, composition (at.%): Al 61.9, O 38.0) with a honeycomb-like microstructure observed on the alloy surface (Region I). YAO et al [12] found that SiO_2 in the ceramic shell forms a liquid phase at high temperatures, which intensifies the local interfacial reaction, leading to the formation of Al_2O_3 and the development of Si-rich "reaction pits" on the casting surface (Region II). Additionally, Ti-rich phases appear as bright white areas in the secondary electron (SE) and backscattered electron (BSD) images. According to the phase analysis results (Fig. 7), the primary phase in these areas is identified as TiO_2.

As shown in Fig. 9(a), the high porosity of the shell surface in the FC sample (Figs. 3 and 4) allows the reaction products to fill in the pores, thereby enhancing the local density of shell surface (Region VI). However, this filling is not uniform, and two distinct forms of Ti-rich phases, blocky and striated, can be observed within the reaction products. EDS analysis at Points 1 and 2 reveals that the blocky structure is composed of TiO_2, while the striated structure is identified as Al_2TiO_5 composite oxides (Table 3). Although the dopant fills in the pores and

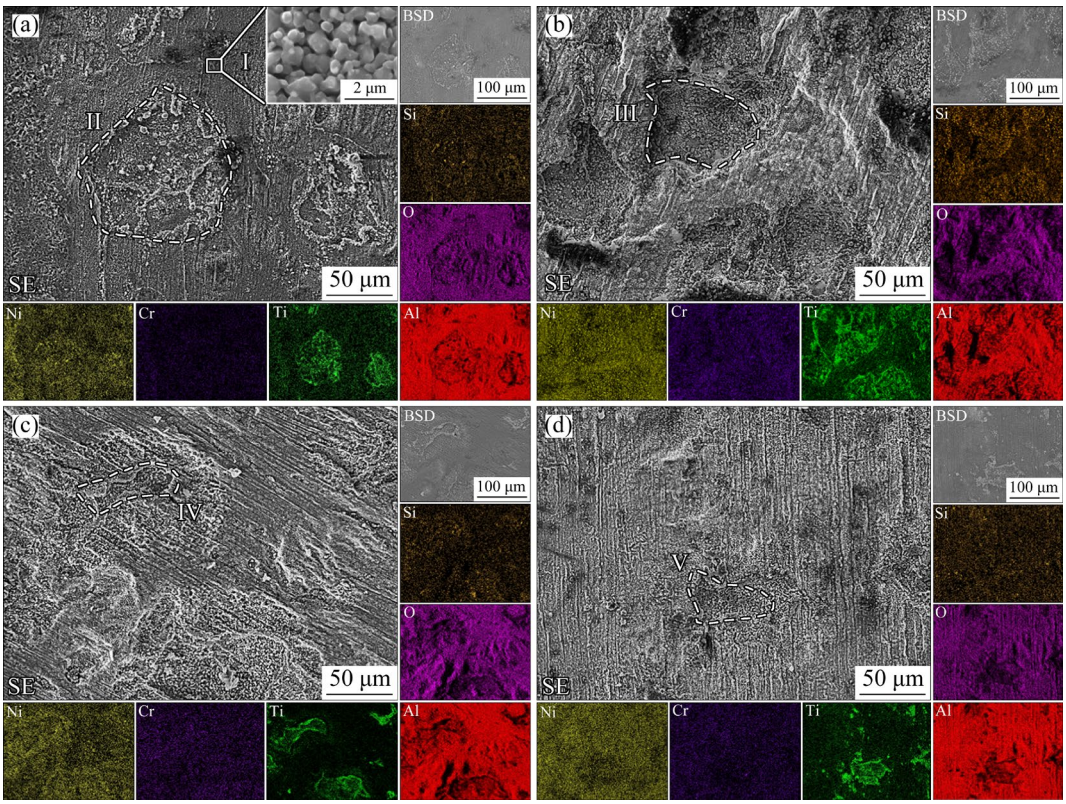

Fig. 8 Micro-morphology and elemental distribution on alloy surface: (a) FC; (b) 8Cr-FC; (c) 8Al-FC; (d) 8Ti-FC

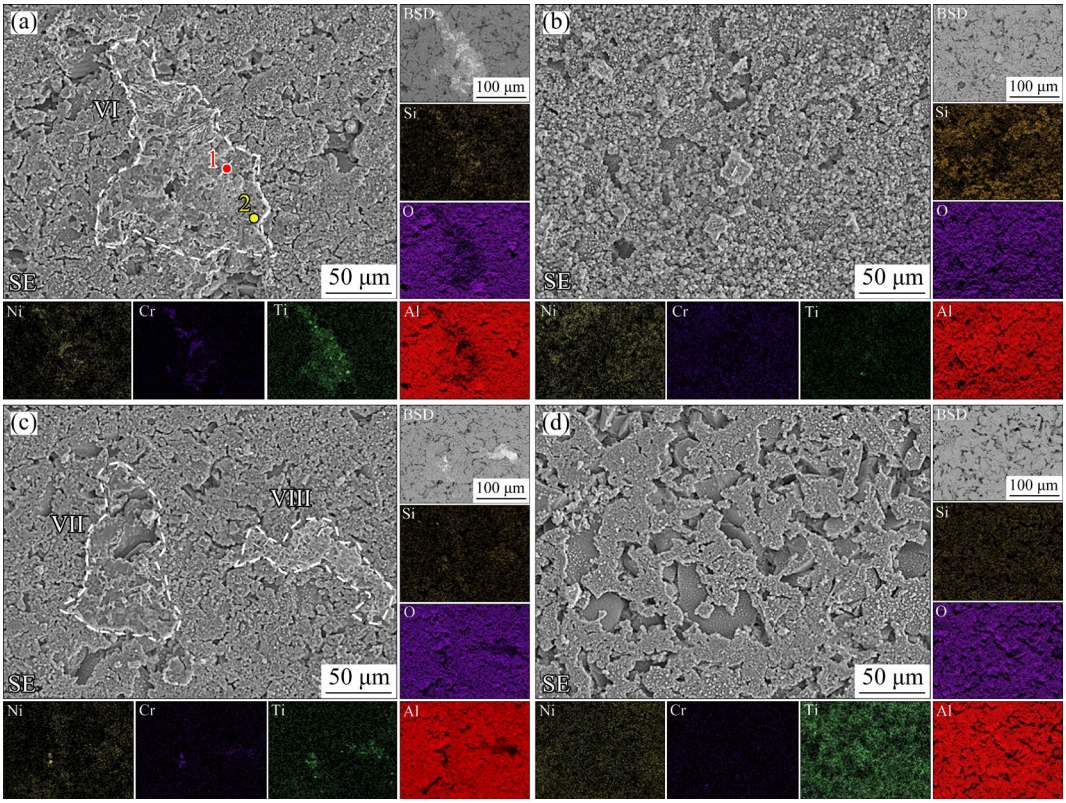

Fig. 9 Micro-morphology and elemental distribution on shell surface: (a) FC; (b) 8Cr-FC; (c) 8Al-FC; (d) 8Ti-FC

Table 3 Element contents in Ti-rich areas of reaction products on shell surface detected by EDS (at.%)

Point No. in Fig. 9	O	Si	Al	Cr	Ti	Co	Mo	Ni
1	62.6	0.6	13.6	1.3	16.7	0.3	4.4	1.5
2	32.4	0.1	5.2	0.4	61.6	–	–	0.3

enhances the density of the shell surface (Figs. 3 and 4), the results indicate that the thermal stability and reaction activity of the dopant in the ceramic shell are more crucial for the interfacial reaction. According to Fig. 1, the thermal stability of the dopants follows the order: Al_2O_3 > TiO_2 > Cr_2O_3. Therefore, Cr_2O_3 dopants can react with Al and Ti elements within the molten alloy. As the Cr_2O_3 content increases, the thickness of the interfacial reaction layer also increases (Figs. 5 and 6), leading to a much rougher alloy surface (Fig. 8(b)) with deeper "reaction pits" (Region III). At the same time, the Cr_2O_3 dopants within the shell surface are largely consumed, compromising the original structure and reducing the surface density (Fig. 9(b)). In the 8Al-FC sample, the alloy surface shows improved smoothness (Fig. 8(c)), and the "reaction pits" become shallower (Region IV). Additionally, the reaction products on the shell surface are less abundant and more dispersed (Fig. 9(c), Regions VII and VIII). This can be attributed to the adoption of Al_2O_3 dopant, which enhances the density and thermal stability of the shell surface, thereby reducing the filling of pores with the reaction products. In the 8Ti-FC sample, the alloy surface achieves the highest degree of smoothness (Fig. 8(d)), as well as fewer and shallower "reaction pits" (Region V). As shown in Fig. 9(d), the shell surface is observed with a layer enriched with Al, Ti, and O elements. This formation is attributed to the TiO_2 dopant, which promotes the formation of Al_2TiO_5 composite oxides within the reaction products and significantly inhibits the interfacial reaction.

The reaction products on the shell surface of FC sample primarily consist of Al_2O_3, TiO_2, $3Al_2O_3{\cdot}2SiO_2$, and $9Al_2O_3{\cdot}Cr_2O_3$, as shown in Fig. 10. In the 8Cr-FC sample, the diffraction peak

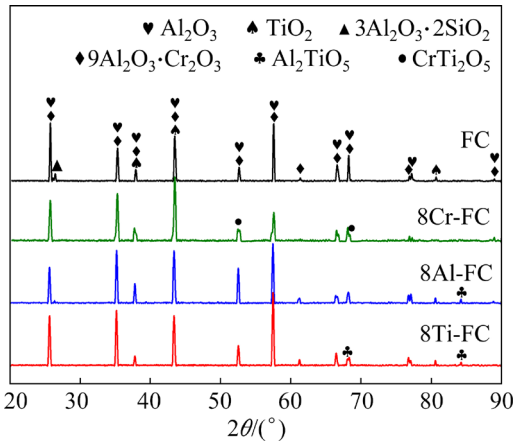

Fig. 10 Phase analysis of reaction products on shell surface

for $3Al_2O_3·2SiO_2$ is absent, while a diffraction peak for the $CrTi_2O_5$ appears. In contrast, the $CrTi_2O_5$ is not observed in the 8Al-FC and 8Ti-FC samples, whereas the Al_2TiO_5 is detected. This confirms that the layer enriched with Al, Ti, and O elements on the shell surface of the 8Ti-FC sample primarily consists of Al_2TiO_5 composite oxides (Fig. 9(d)).

3.4 Cross-sectional microstructure and elemental distribution of interfacial reaction layer

Figure 11 shows the micro-morphology and elemental distribution in the interfacial reaction layer on the alloy surfaces of the FC, 8Cr-FC, 8Al-FC, and 8Ti-FC samples. The alloy matrix primarily consists of Ni and other elements. The reaction products primarily consist of Si, O, Al, and Ti elements. Al and O form a continuous Al_2O_3 layer within the reaction products. Si is observed to diffuse into the reaction products due to a displacement reaction between the active metal elements in the molten alloy and the SiO_2 of the shell surface. Ti is observed outside the Al_2O_3 layer, which is attributed to the presence of TiO_2 above the Al_2O_3 layer (Figs. 7 and 8). No obvious Cr-rich area is observed in the reaction products, indicating that $9Al_2O_3·Cr_2O_3$ composite oxides are absent in the interfacial reaction layer, but should exist in the sticking sand.

The elemental distribution in the alloy matrix and the interfacial reaction layer was further investigated through EDS spectra with line scan model. The test position and scanning direction are shown in Fig. 11, and the test results are shown in Fig. 12. The intersection points of the Al and Ni signal intensities between the alloy matrix and the interfacial reaction layer indicate significant compositional differences in these two sides. As shown in Fig. 12(a), the interfacial reaction layer in the FC sample is mainly composed of O, Si, Ti, and Al. An Al_2O_3 layer with a thickness of about 2.9 μm is located on the alloy matrix, with Si and Ti located outside Al_2O_3 layer. The active metal elements Cr, Al, and Ti are consumed during the interfacial reaction, leading to a relative increase in the Co and Mo content on the surface of the alloy matrix. In the 8Cr-FC sample (Fig. 12(b)), the Cr content within the alloy matrix shows a significant increase, confirming that the Cr_2O_3 dopant can inhibit the diffusion of Cr from the alloy matrix to interfacial

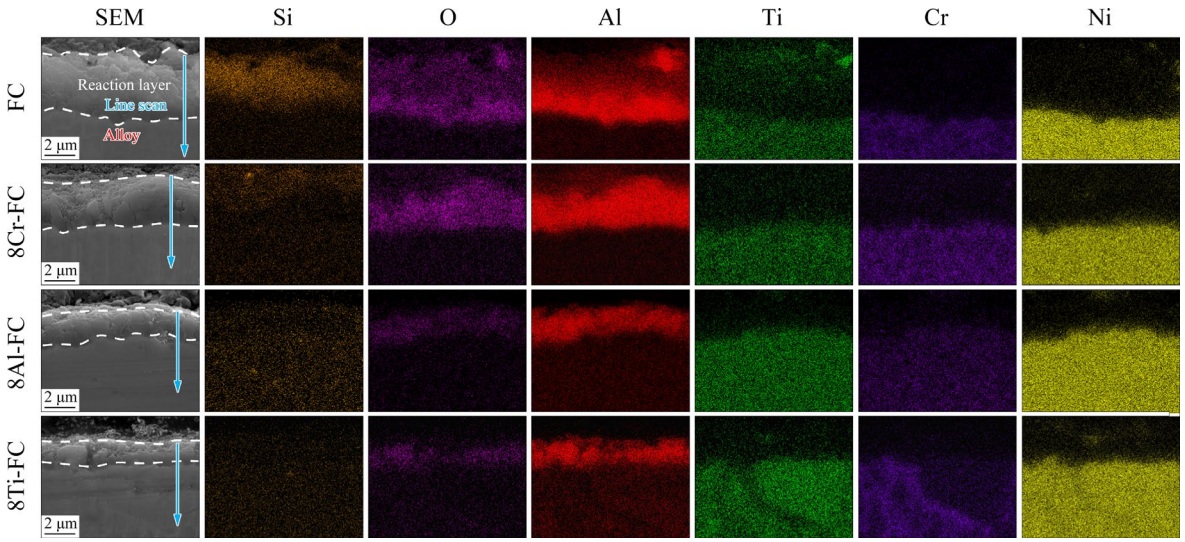

Fig. 11 Micro-morphology and elemental distribution in interfacial reaction layer on alloy surface (Arrows in the first column indicate the EDS line scan traces)

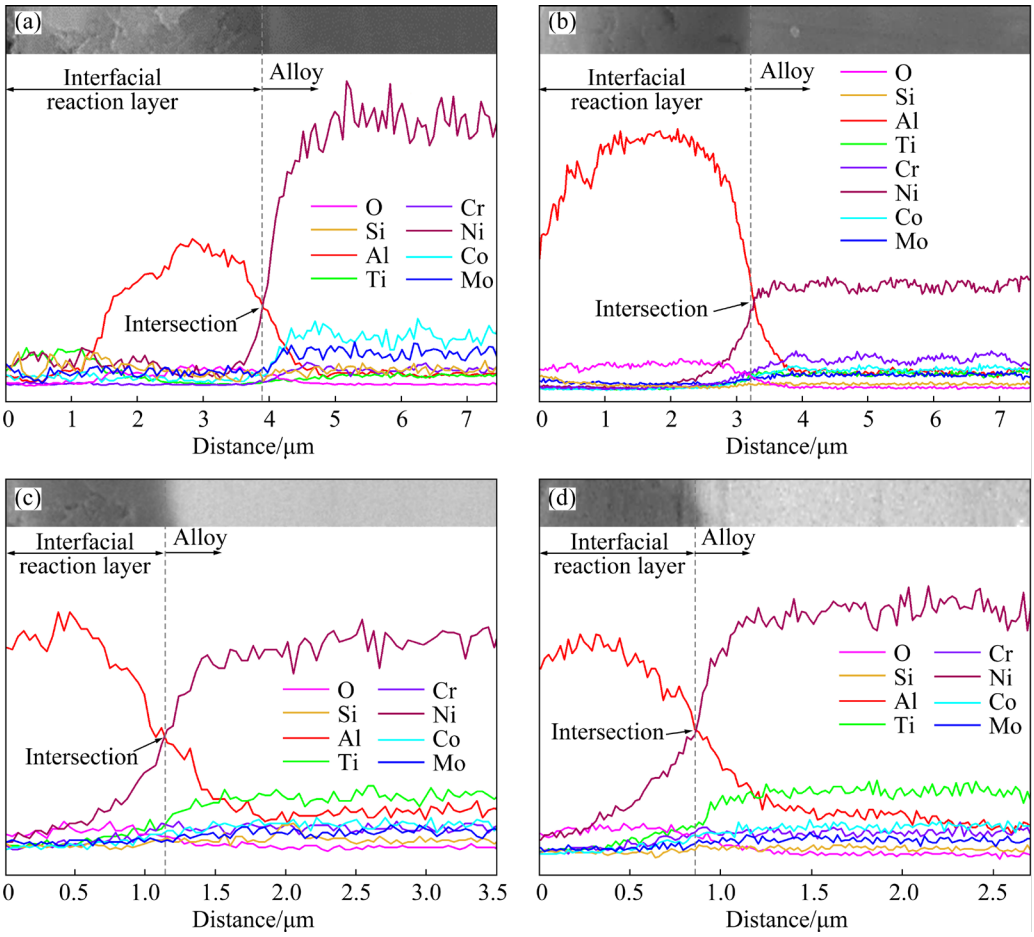

Fig. 12 EDS line scan results from interfacial reaction layer to alloy matrix: (a) FC; (b) 8Cr-FC; (c) 8Al-FC; (d) 8Ti-FC

reaction layer. However, due to the instability of Cr_2O_3 dopant, it further reacts with Al and Ti in the alloy matrix, leading to a reduction in their content within the alloy matrix and an increase in the thickness of Al_2O_3 layer to over 3 μm. In 8Al-FC sample (Fig. 12(c)), the content of Al and Ti in the alloy matrix increases, while the thickness of the Al_2O_3 layer is about 1.2 μm. In the 8Ti-FC sample (Fig. 12(d)), the Ti content in the alloy matrix further increases, and the thickness of the Al_2O_3 layer is less than 1 μm. It should be noted that the thickness of the interfacial reaction layer is not uniform and has a margin of error (Figs. 5(b) and 6(b)). Thus, the thickness measured in the EDS line scan results is less than the average value.

3.5 Role of dopant type and content on wettability

Under ideal conditions (a smooth solid surface and non-reactive solid−liquid interface), wettability characterization follows Young's three-phase equilibrium equation (Eq. (4)) [30]. For non-smooth solid surfaces, the Wenzel equation (Eq. (5)) [31] is applicable:

$$\cos\theta_0=(\sigma_{sv}-\sigma_{ls})/\sigma_{lv} \quad (4)$$

$$\cos\theta_1=m(\sigma_{sv}-\sigma_{ls})/\sigma_{lv} \quad (5)$$

where θ_0 is the wetting angle on a smooth solid surface; σ_{sv}, σ_{ls} and σ_{lv} represent the surface tensions of ceramic/steam, alloy/ceramic, and alloy/steam, respectively; θ_1 is the wetting angle on a rough solid surface; m is the roughness factor of solid surface. Since $m > 1$, it follows $\cos\theta_1 > \cos\theta_0$. Therefore, if the actual contact angle is less than 90°, then $\theta_1 < \theta_0$. The greater the roughness, the higher the m value, leading to a smaller measured wetting angle and improved wettability of the molten alloy on the ceramic shell. Conversely, if the actual contact angle exceeds 90°, increased surface roughness results in a larger wetting angle and decreased wettability [26]. Based on the above conditions, as the dopant content increases, the porosity and roughness of the shell surface decrease (Figs. 3 and 4). Therefore, assuming no interfacial reaction occurs, the wetting angle is expected to decrease as well.

In this study, the dopants have a significant impact on both the wettability and interfacial reaction (Figs. 5 and 6). According to the theory of wettability changes during interfacial reactions [32], a strong interfacial reaction is essential for achieving good wettability. The more intense the interfacial reaction, the greater the wettability, leading to a smaller wetting angle. Conversely, when the interfacial reaction is inhibited, the wettability deteriorates, resulting in an increased wetting angle. In the FC sample, the wetting angle is about 95°, indicating a non-wetting relationship between the alloy and the shell [33]. As the Cr_2O_3 dopant content increases, the interfacial reaction intensifies, leading to an increase in the thickness of the interfacial reaction layer and a decrease in the wetting angle. Conversely, as the contents of Al_2O_3 and TiO_2 dopants increase, the interfacial reaction is inhibited, leading to a thinner interfacial reaction layer and a larger wetting angle.

3.6 Role of dopant type and content on interfacial reaction

Three main mechanisms of reactive wetting have been identified [16]: solution-driven wetting, interfacial adsorption-driven wetting, and interfacial reaction-driven wetting. As shown in Fig. 13, the interfacial reaction between K417G superalloy and Al_2O_3-based ceramic shell can be divided into four primary steps [33]: (1) liquefaction or decomposition of the ceramic shell material, (2) diffusion of atoms from the decomposed shell to alloy/shell interface, (3) diffusion of active atoms from the alloy matrix to alloy/shell interface, and (4) the occurrence of interfacial reaction at the alloy/shell interface. Thus, the interfacial reaction in this system can be categorized into the following types [34]:

$$M_xO(s)=M_xO \quad (6)$$

$$M_xO=x[M]+[O] \quad (7)$$

$$y[N]+[O]=N_yO \quad (8)$$

$$y[N]+M_xO=N_yO+x[M] \quad (9)$$

where M_xO represents the oxides in ceramic shell, including Al_2O_3, SiO_2, and dopants. "N" represents the active metal elements in the alloy matrix. According to Figs. 1 and 7, the active metal elements involved in the interfacial reaction are Al, Ti, and Cr. Before the interfacial reaction occurs, the active elements in the alloy gather and adsorb at the alloy/shell interface [16] (Fig. 13(a)). When the critical concentration or temperature is reached, the interfacial reaction occurs, leading to the formation of reaction products at the interface. The thermal erosion caused by the molten alloy is the primary factor driving the liquefaction and decomposition of the shell materials (Eqs. (6) and (7)), and thus the density of the shell surface significantly influences the thermal erosion. The thermal stability of oxides in the interfacial system follows the order: Al_2O_3 > TiO_2 > SiO_2 > Cr_2O_3 (Fig. 1). Therefore, Al and Ti in the alloy exhibit stronger oxidation abilities (Eq. (8)) and can undergo displacement reactions with SiO_2 and Cr_2O_3, resulting in the formation of more stable

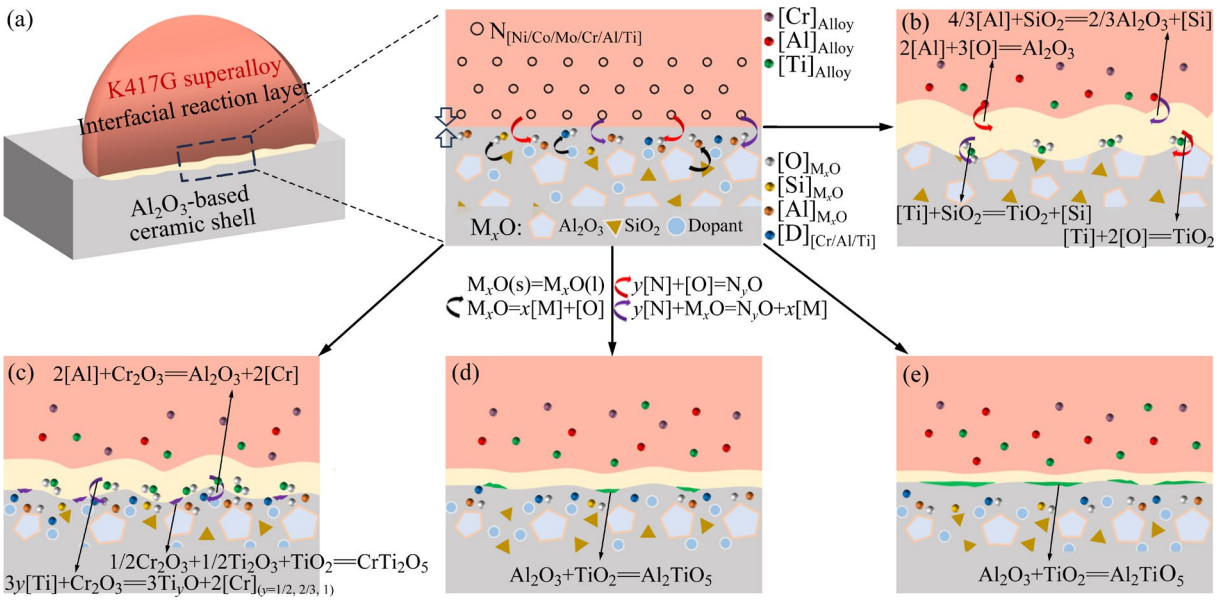

Fig. 13 Diagram of interfacial reaction: (a) Interfacial reaction system; (b) FC; (c) 8Cr-FC; (d) 8Al-FC; (e) 8Ti-FC

oxides (Eq. (9)). Figure 14 shows the XPS spectra obtained from the alloy surface in the FC, 8Cr-FC, 8Al-FC, and 8Ti-FC samples. The chemical states of the elements Al, Ti, Cr, and Si were determined by deconvolving their corresponding detailed XPS scan spectra [16,35−37]. This analysis provides a more detailed and accurate understanding of the interfacial reaction processes. The reaction products primary include Al_2O_3 (Al^{3+}), TiO_2 (Ti^{4+}), Cr_2O_3 (Cr^{3+}), SiO_2, and SiO_x (Si^{4+}, $0<x<2$). In this case, SiO_x is generated by the reaction of Si with atmospheric O_2 during the cooling process at the end of the experiment. Additionally, a peak observed at 581.5 eV corresponds to Cr^{6+}. According to Ref. [37,38], the oxidation state transition from Cr^{3+} to Cr^{6+} is likely attributed to charge balance considerations. Although there is a possibility of forming trace amounts of chromates, their quantities are insufficient to produce distinct diffraction peaks in the XRD pattern (Fig. 7).

In the FC sample, the density of the shell surface is the lowest, leading to intense liquefaction and decomposition under thermal erosion by the molten alloy (Eqs. (6) and (7)). This increases the oxygen concentration at the interface, resulting in the most severe interfacial reaction (Figs. 5(b) and 13(b)). Although the increase in dopant content enhances the density of the shell surface (Fig. 3), the thermal stability of the dopant significantly affects the extent of interfacial reaction. When the Cr_2O_3 dopant content is 2 wt.%, the interfacial reaction layer is thinner compared to that of the FC sample.

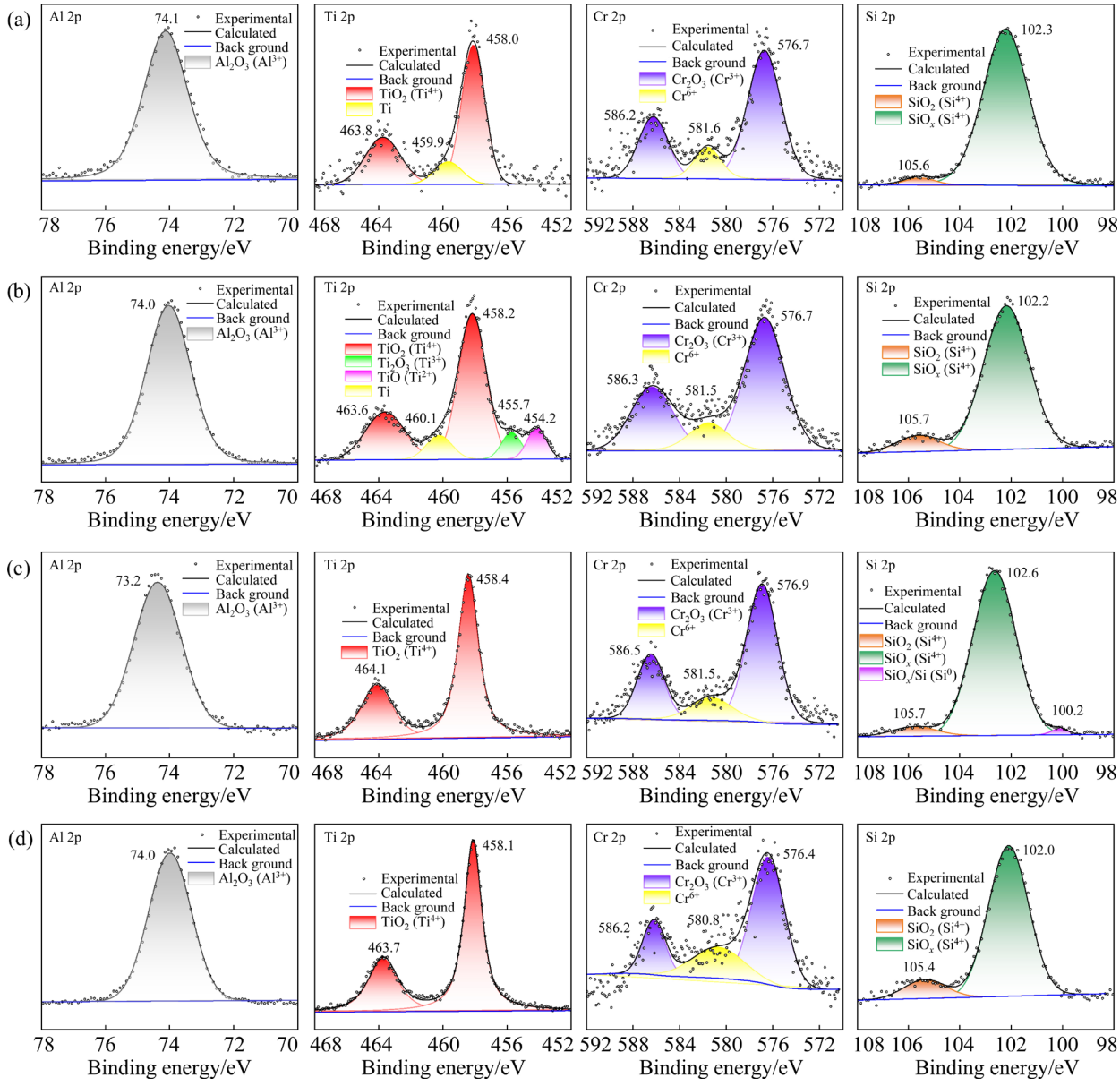

Fig. 14 XPS spectra of alloy surface: (a) FC; (b) 8Cr-FC; (c) 8Al-FC; (d) 8Ti-FC

This reduction can be attributed to the formation of Al_2O_3−Cr_2O_3 or Al_2O_3−SiO_2−Cr_2O_3 composite oxides, which inhibit the interfacial reaction [22]. However, as the Cr_2O_3 dopant content increases (2−8 wt.%), a displacement reaction between Cr_2O_3 dopants and the Al and Ti in the molten alloy intensifies (Eq. (9)), leading to an increase in the thickness of the interfacial reaction layer and a decrease in the wetting angle (Figs. 12(b) and 13(c)). Notably, the reaction products in the 8Cr-FC samples exhibit complex valence states of Ti, including Ti (Ti^{0+}), TiO (Ti^{2+}), Ti_2O_3 (Ti^{3+}), and TiO_2 (Ti^{4+}), as shown in Fig. 14(b). The ΔG of the potential chemical reaction within the interfacial system at 1623 K is calculated to evaluate the thermodynamic feasibility of these reactions, as detailed in the literature [39] and Eq. (10):

$$\Delta G^{\Theta}(T)=\Delta H^{\Theta}_{298\ \mathrm{K}}-T\Delta S^{\Theta}_{298\ \mathrm{K}}+\int_{298\ \mathrm{K}}^{T}\Delta c_p\mathrm{d}T-T\int_{298\ \mathrm{K}}^{T}\frac{\Delta c_p}{T}\mathrm{d}T \tag{10}$$

where $\Delta G^{\Theta}(T)$ represents the standard Gibbs free energy change of the chemical reaction at temperature T, $\Delta H^{\Theta}_{298\ \mathrm{K}}$ is the standard enthalpy of formation of the chemical reaction, $\Delta S^{\Theta}_{298\ \mathrm{K}}$ is the standard entropy of the chemical reaction, and Δc_p refers to the sum of the constant pressure heat capacities of the substances involved in the chemical reaction. The calculated results are presented in Table 4. For every 1 mol of Cr_2O_3 consumed, the ΔG for formation of Ti oxides is as follows: 0 > TiO_2 > Ti_2O_3 > TiO. Therefore, at 1623 K, all these reactions are feasible, leading to a diversity of Ti valence states in the reaction products. Thus, the equation for the formation of the $CrTi_2O_5$ composite oxides may take place as follows:

$$1/2Cr_2O_3+1/2Ti_2O_3+TiO_2=CrTi_2O_5 \tag{11}$$

Table 4 Gibbs free energy change (ΔG) for displacement reaction between Ti and Cr_2O_3 at 1623 K

Reaction	ΔG/(kJ·mol^{-1})
$3/2Ti+Cr_2O_3=3/2TiO_2+2Cr$	−262.445
$2Ti+Cr_2O_3=Ti_2O_3+2Cr$	−365.282
$3Ti+Cr_2O_3=3TiO+2Cr$	−455.504

In the Al-FC and the Ti-FC samples, the interfacial reaction is significantly inhibited by three factors: (1) The dopant increases both the density and high-temperature stability of the shell surface, thereby reducing thermal erosion from the molten alloy; (2) The dopants reduce the diffusion of active metal elements to the interfacial reaction layer; (3) The Al_2TiO_5 composite oxides are formed. Compared to Al_2O_3, TiO_2 dopants are more favorable for the formation of Al_2TiO_5 composite oxides on the shell surface (Figs. 9(d) and 13(e)), which can be formed as follows:

$$Al_2O_3+TiO_2=Al_2TiO_5 \tag{12}$$

4 Conclusions

(1) Al, Ti, and Cr are critical elements in the interfacial reaction of the K417G superalloy. Their oxides (Al_2O_3, TiO_2, Cr_2O_3) have significant effect on property of the Al_2O_3-based ceramic shell.

(2) Appropriate dopants should enhance the surface packing density of the shell surface. As the content of Al_2O_3 dopant increases (0−8 wt.%), both the surface porosity (21.74%−10.08%) and the roughness (3.22−1.34 μm) decrease.

(3) The dopants can suppress the diffusion of active metal elements from the alloy matrix to the interface, thereby increasing their concentration at the surface of the alloy matrix.

(4) The poor thermal stability of the Cr_2O_3 dopant leads to displacement reactions with Al and Ti in the molten alloy. Increasing its content intensifies the interfacial reaction and decreases the wetting angle.

(5) Al_2O_3 and TiO_2 dopants can enhance the thermal stability of the shell surface, reduce thermal erosion caused by the molten alloy, and promote the formation of Al_2TiO_5 composite oxides within the reaction products. This effectively inhibits the interfacial reaction and increases the wetting angle.

CRediT authorship contribution statement

Bao-hong KOU: Conceptualization, Methodology, Investigation, Writing − Original draft preparation; **Wen-tao ZHOU:** Investigation; **Yong-hui PENG:** Methodology; **Jing OUYANG:** Supervision, Writing − Review & editing.

Declaration of competing interest

The authors declare that they have no known competing financial interests or personal relationships that could have appeared to influence the work reported in this paper.

Acknowledgments

This work was supported by the National Natural Science Foundation of China (No. 52374292), China Baowu Low Carbon Metallurgy Innovation Foundation, China (No. BWLCF202309), and the Natural Science Foundation of Changsha City, China (No. KQ2208271).

References

[1] CHEAH C M, CHUA C K, LEE C W, FENG C, TOTONG K. Rapid prototyping and tooling techniques: A review of applications for rapid investment casting [J]. International Journal of Advanced Manufacturing Technology, 2005, 25: 308−320.

[2] KANYO J E, SCHAFFONER S, UWANYUZE R S, LEARY K S. An overview of ceramic molds for investment casting of nickel superalloys [J]. Journal of the European Ceramic Society, 2020, 40: 4955−4973.

[3] WANG Kai-meng, JING Hong-yang, XU Lian-yong, ZHAO Lei, HAN Yong-dian, LI Hai-zhou, SONG Kai. Microstructure evolution of 55Ni−23Cr−13Co nickel-based superalloy during high-temperature cyclic deformation [J]. Transactions of Nonferrous Metals Society of China, 2021, 31: 3452−3468.

[4] LI H, CHANDRASHEKHARA K, KOMARAGIRI S, LEKAKH S N, RICHARDS V L. Crack prediction using nonlinear finite element analysis during pattern removal in investment casting process [J]. Journal of Materials Processing Technology, 2014, 214: 1418−1426.

[5] WANG Zhi-cheng, LI Jia-rong, LIU Shi-zhong, YANG Wan-peng, WANG Xiao-guang. Effects of shell mold heating temperature on microstructures and freckle formation of single crystal superalloys [J]. Transactions of Nonferrous Metals Society of China, 2024, 34: 1191−1203.

[6] SONG Ruo-kang, MA Dong, WU Su-jun. Mechanical properties and thermal fatigue behavior of K417G superalloy used in turbine guide vane [J]. Rare Metal Materials and Engineering, 2019, 48: 1517−1522. (in Chinese)

[7] YE Wen-ming, HU Xu-teng, SON Ying-dong. The relationship between creep and tensile properties of a nickel-based superalloy [J]. Materials Science and Engineering A, 2020, 774: 138847−138847.

[8] LUO Yao-feng, LU Rui-yu, WANG Yan, LIU Bin, YANG Hai-tang, LIU Yong. Interfacial reaction in Al_2O_3 fiber reinforced TiAl matrix composite [J]. Transactions of Nonferrous Metals Society of China, 2023, 33: 2054−2063.

[9] LI Xiao-ya, ZOU Jian-peng, SHI Qian, DAI Ming-jiang, YANG Hong-zhi, LIN Song-sheng, ZHANG Cheng, LIU Ying-kun, TANG Peng, SU Yi-fan. Microstructural evolution and element interdiffusion of NiAlHf and NiAlHfY coatings deposited on a Ni-based superalloy [J]. Surface & Coatings Technology, 2022, 451: 129075.

[10] LI Qing, SONG Jin-xia, WANG Ding-gang, YU Qian, XIAO Cheng-bo. Effect of Cr, Hf and temperature on interface reaction between nickel melt and silicon oxide core [J]. Rare Metals, 2011, 30: 405−409.

[11] SONG Qing-zhong, QIAN Kun, SHU Lei, CHEN Bo, MA Ying-che, LIU Kui. Interfacial reaction between nickel-based superalloy K417G and oxide refractories [J]. Acta Metallurgica Sinica, 2022, 58: 868−882. (in Chinese)

[12] YAO Jian-sheng, TANG Ding-zhong, LI Xin, CHENG Xiao-bo, LIU Xiao-guang, ZHOU Han-kun. Interface reactions between Al_2O_3 shells and DZ22 surperalloy [J]. Special-cast and Non-ferrous Alloys, 2014, 34: 630−633. (in Chinese)

[13] YAO Jian-sheng, TANG Ding-zhong, LIU Xiao-guang, XIAO Cheng-bo, LI Xin, CAO Chun-xiao. Interaction between two Ni-base alloys and ceramic moulds [J]. Materials Science Forum, 2013, 2233: 765−771.

[14] EUSTATHOPOULOS N, DREVET B. Relationship between reactivity and wettability in metal/oxide systems [J]. Composite Interfaces, 2012, 2: 29−42.

[15] ZI Yun, MENG Jie, ZOU Ming-ke, XU Wei, LI Jin-guo, XU Ke, ZHOU Yi-zhou, DING Yu-tian. Effects of yttrium on wettability and interactions between molten superalloy and SiO_2-based ceramic core [J]. Ceramics International, 2020, 46: 7324−7335.

[16] LI Yi, TAN Yi, WANG Ding-gang, LI Peng-ting, CHEN Ziang, ZHAO Jia-qi, QIANG Jian-bing. Effect of trace impurity elements on the wettability and interfacial reaction between DZ125 alloy and ceramic shell [J]. Corrosion Science, 2023, 221: 111370.

[17] ZI Yun, MENG Jie, ZHANG Chao-wei, YANG Yan-hong, ZHOU Yi-zhou, DING Yu-tian. Effect of Y content on interface reaction and wettability between a nickel-base single crystal supermolten alloy and ceramic mould [J]. Journal of Alloys and Compounds, 2019, 789: 472−484.

[18] ZI Yun, MENG Jie, ZHANG Chao-wei, ZHOU Yi-zhou, DING Yu-tian. Mechanisms of rhenium on wettability and interactions between nickel-base supermolten alloy and Al_2O_3-based ceramic material [J]. Acta Metallurgica Sinica (English Letters), 2020, 33: 1−10.

[19] CHEN Yan-fei, XIAO Shu-long, TIAN Jing, XU Li-juan, CHEN Yu-yong. Effect of particle size distribution on properties of zirconia ceramic mould for TiAl investment casting [J]. Transactions of Nonferrous Metals Society of China, 2011, 21: s342−s347.

[20] VENKAT Y, SINGH S, DAS D K, PANDEY A K. Effect of fine alumina in improving refractoriness of ceramic shell moulds used for aeronautical grade Ni-base superalloy castings [J]. Ceramics International. 2018, 44: 12030−12035.

[21] ДЕМОНИС И М, КАРПОВИЧ Ю Ф, ГЛЕЗЕР Г М, РЕФЕРАТ. Interaction between ceramics and molten alloys during directional solidification [J]. Journal of Aeronautical Materials, 1991(S1): 62−63. (in Chinese)

[22] SHI Zhen-wei, ZHENG Wei, LU Yu-zhuang, ZHANG Gong, SHEN Jian. Sand-burning reaction of ceramic shell for directional solidification of nickel-based superalloy [J]. Chinese Journal of Materials Research, 2021, 35: 251−258. (in Chinese)

[23] TENG Jian-wei, GONG Xiao-juan, YANG Biao-biao, YU Shu, LAI Rui-lin, LIU Jian-tao, LI Yun-ping. High temperature oxidation behavior of a novel Ni−Cr−W−Al−Ti superalloy [J]. Corrosion Science, 2022, 198: 110141.

[24] TENG Jian-wei, GONG Xiao-juan, YANG Biao-biao, YU Shu, LIU Jian-tao, LI Yun-ping. Influence of Ti addition on

oxidation behavior of Ni−Cr−W-based superalloys [J]. Corrosion Science, 2021, 193: 109882.
[25] CONFALONIERI C, CAMNAGHI A, GARIBOLDI E. Design of fully-metallic phase change composites from thermodynamic calculations to experimental characterization of form-stable systems [J]. Transactions of Nonferrous Metals Society of China, 2024, 34: 1393−1412.
[26] CHEN Zhao-you. Thermodynamics of refractories [M]. Beijing: Metallurgical Industry Press, 2005. (in Chinese)
[27] CHEN J. Handbook of commonly used charts and data in steelmaking [M]. Beijing: Metallurgical Industry Press, 2010. (in Chinese)
[28] GONG Li, CHEN Bo, Du Zhan-hui, ZHANG Meng-shu, LIU Rui-chang, LIU Kui. Investigation of solidification and segregation characteristics of cast Ni-base superalloy K417G [J]. Journal of Materials Science & Technology, 2018, 34: 541−550.
[29] LIU Shi-yuan, XUE Wei-hua, WANG Li-jun, CHOU Kuo-chih. Synthesis of mullite by high temperature reaction to realize nontoxic and efficient recycling of vanadium slag chlorination residue [J]. Transactions of Nonferrous Metals Society of China, 2023, 33: 2523−2534.
[30] CHEN Ming-hai, LIU Ning, XU Yu-dong. Development of research on the wettability of metal on ceramics [J]. Cemented Carbide, 2002, 04: 199−205. (in Chinese)
[31] LIU Huai-dong, LIU Da-you, LI Peng-hu, ZENG Yong-jie, JIN Hai-yun. Direct observation of the wetting state of Cassie and Wenzel [J]. Materials Letters, 2023, 340: 134182.
[32] SAIZ E, CANNON R M, TOMSIA A P. Reactive spreading: Adsorption, ridging and compound formation [J]. Acta Materialia, 2000, 48: 4449−4462.
[33] SOBCZAK N, SINGH M, ASTHANA R, High-temperature wettability measurements in metal/ceramic systems-some methodological issues [J]. Current Opinion in Solid State & Materials Science, 2005, 9: 241−253.
[34] JAFARI H, IDRI M H, OURDJINI A. A review of ceramic shell investment casting of magnesium alloys and mold-metal reaction suppression [J]. Materials and Manufacturing Processes, 2013, 28: 843−856.
[35] RUMBLE J R, BICKHAM D M, POWELL C J. The NIST X-ray photoelectron spectroscopy database [J]. Surface and Interface Analysis, 1992, 19: 241−246.
[36] PAN Yu, YANG Yu-cheng, ZHOU Qing-jun, QU Xuan-hui, CAO Peng, LU Xin. Achieving synergy of strength and ductility in powder metallurgy commercially pure titanium by a unique oxygen scavenger [J]. Acta Materialia, 2024, 263: 119485.
[37] CHENG Si, JIANG Feng, FENG Guo, LIU Jian-min, LIANG Jian, MIAO Li-feng, BAO Zhen-hong, YU Yong-zhi. Low-temperature synthesis of ultrafine Cr, Mg-codoped Al_2TiO_5 nanocrystals as high-temperature green ceramic pigment [J]. Ceramics International, 2023, 49: 22110−22117.
[38] ZHANG Zu-de. Inorganic chemistry [M]. Revised Edition: Hefei: University of Science and Technology of China Press, 2010. (in Chinese)
[39] LIANG Ying-jiao, CHE Meng-chang. Thermochemical data of inorganics [M]. Shenyang: Northeastern University Press, 1993. (in Chinese)

活性金属氧化物掺杂剂对 K417G 高温合金与 Al_2O_3 基陶瓷型壳润湿性及界面反应的影响

寇宝弘[1,2,3]，周文韬[1,2,3]，彭勇慧[1,2,3]，欧阳静[1,2,3]

1. 中南大学 资源加工与生物工程学院 无机材料系，长沙 410083；
2. 中南大学 矿物材料及其应用湖南省重点实验室，长沙 410083；
3. 中南大学 金属资源开发利用碳减排教育部工程研究中心，长沙 410083

摘　要：选用活性金属氧化物(Al_2O_3、TiO_2、Cr_2O_3) 作为 K417G 高温合金熔模铸造用 Al_2O_3 基陶瓷型壳的掺杂剂，通过固滴实验研究了掺杂剂种类及含量(0、2、5、8，质量分数，%)对合金型壳的润湿性和界面反应的影响。结果表明，随着 Al_2O_3 掺杂剂含量的增加(0~8%，质量分数)，型壳表面的孔隙率(21.74%~10.08%)和粗糙度(3.22~1.34 μm)均减小。随着 Cr_2O_3 含量的增加(2%~8%，质量分数)，界面反应加剧，界面反应层厚度增大(2.6~3.1 μm)，润湿角减小(93.9°~91.0°)。Al_2O_3 和 TiO_2 掺杂剂使反应产物中生成 Al_2TiO_5 复合氧化物，有效抑制界面反应。TiO_2 掺杂剂含量的增加(0~8%，质量分数)，进一步促进了 Al_2TiO_5 的生成，使界面反应层厚度减小(3.9~1.2 μm)，润湿角增大(95.0°~103.8°)。掺杂剂颗粒在提高型壳表面的堆积密度的同时抑制活性金属元素从合金基体向界面的扩散。

关键词：Al_2O_3 基陶瓷型壳；K417G 高温合金；金属氧化物掺杂剂；界面反应；润湿性

(Edited by Bing YANG)